# Synthesis of Tin and Tin Oxide Nanoparticles of Low Size Dispersity for Application in Gas Sensing

**Céline Nayral,[a] Eric Viala,[a] Pierre Fau,[b] François Senocq,[c] Jean-Claude Jumas,[d] André Maisonnat,*[a] and Bruno Chaudret*[a]**

**Abstract:** Nanocomposite core–shell particles that consist of a $Sn^0$ core surrounded by a thin layer of tin oxides have been prepared by thermolysis of $[\{Sn(NMe_2)_2\}_2]$ in anisole that contains small, controlled amounts of water. The particles were characterized by means of electronic microscopies (TEM, HRTEM, SEM), X-ray diffraction (XRD) studies, photoelectron spectroscopy (XPS), and Mössbauer spectroscopy. The TEM micrographs show spherical nanoparticles, the size and size distribution of which depends on the initial experimental conditions of temperature, time, water concentration, and tin precursor concentration. Nanoparticles of 19 nm median size and displaying a narrow size distribution have been obtained with excellent yield in the optimized conditions. HRTEM, XPS, XRD and Mössbauer studies indicate the composite nature of the particles that consist of a well-crystallized tin $\beta$ core of $\approx$11 nm covered with a layer of $\approx$4 nm of amorphous tin dioxide and which also contain quadratic tin monoxide crystallites. The thermal oxidation of this nanocomposite yields well-crystallized nanoparticles of $SnO_2$ without coalescence or size change. XRD patterns show that the powder consists of a mixture of two phases: the tetragonal cassiterite phase, which is the most abundant, and an orthorhombic phase. In agreement with the small $SnO_2$ particle size, the relative intensity of the adsorbed dioxygen peak observed on the XPS spectrum is remarkable, when compared with that observed in the case of larger $SnO_2$ particles. This is consistent with electrical conductivity measurements, which demonstrate that this material is highly sensitive to the presence of a reducing gas such as carbon monoxide.

**Keywords:** colloids · nanostructures · semiconductors · sensors · tin

## Introduction

The optical and electrical properties of polycrystalline semiconducting oxides depend strongly on the surface states of the individual grains, and on the distribution and the nature of the grain boundaries. Thus, the non-linear resistivity of zinc oxide varistors is partially explained in terms of chemisorption and diffusion of dioxygen to the grain boundaries, [1–3] a phenomenon which is generally treated as an electronic process in which charge transfer occurs between the adsorbed species and the oxide.[4, 5] Similarly, the changes in electric conductivity of the semiconducting oxide gas sensors involve redox processes that result from the interaction of reducing gases with surface oxygens. This gives rise to a measurable signal.[6–8] In nanosized materials, since the surface to volume ratio is much larger than that commonly found for semiconductor materials, both the surface properties and the grain-boundary distribution become predominant. This renders these materials as good candidates for applications that will take advantage of the high surface/volume ratio, such as chemical sensors [9–12] or luminescent semiconducting sensors.[13]

The precise control of the morphology of semiconducting oxide materials at a nanometric scale is consequently of basic importance and, given the industrial and commercial demands, requires reproducible low-cost synthetic methods that can be implemented in microelectronic processes. Concerning tin dioxide, the oxide material most widely used as the sensitive layer of chemical sensors,[6–8] several synthetic

[a] Dr. A. Maisonnat, Dr. B. Chaudret, Dr. C. Nayral, E. Viala[+]
Laboratoire de Chimie de Coordination du CNRS, UPR 8241
205 route de Narbonne, 31077 Toulouse Cedex 04 (France)
Fax: (+33) 561-55-30-03
E-mail: maisonat@lcc-toulouse.fr
chaudret@lcc-toulouse.fr

[b] Dr. P. Fau
MicroChemical System SA, 15 rue de Porcena
Corcelles, 2035 (Switzerland)

[c] Dr. F. Senocq
Laboratoire Interface et Matériaux
Ecole Nationale Supérieure de Chimie, INPT
118, route de Narbonne, 31077 Toulouse Cedex 04 (France)

[d] Dr. J.-C. Jumas
Laboratoire des Agrégats Moléculaires et
Matériaux Inorganiques (ESA 5072 CNRS) Université Montpellier II
Sciences et Technologies du Languedoc, Case Courrier 015
Place E. Bataillon, 34095 Montpellier Cedex 5 (France)

[+] E.V. on leave from Motorola Semiconductors SA, le Mirail, BP 1029, 31023 Toulouse Cedex 4 (France)



0947-6539/00/0622-4082 $ 17.50+.50/0

methods are available. The most common methods involve physical processes such as sputtering from a tin oxide target,[14–16] sputtering from a metallic target followed by oxidation,[17–19] which includes the RGTO method (rheotaxial growth and thermal oxidation),[20] thermal evaporation of tin[21] or tin oxide,[22] laser ablation of ceramic samples,[23, 24] and chemical vapor decomposition.[25, 26] Alternative chemical processes include the widely used sol-gel technique.[9, 10, 27–33] These processes generally lead to polycrystalline materials that are subjected to subsequent thermal treatments, which are aimed at improving the stability of the materials and the reproducibility of the preparation. However, thermal treatments lead to an increase of the average grain size, spreading of the grain size distribution[30, 34, 35] and changes in the phase composition[36] with increasing annealing temperature.

As an alternative method to prepare $SnO_2$ nanoparticles displaying a low size dispersity, we have considered the use of organometallic precursors. We have previously shown that the synthesis of nanoparticles of controlled size, composition, and surface could be achieved by decomposition of organometallic precursors in the presence of a reactive gas in mild conditions. This method has been applied to the preparation of noble metal particles[37–39] as well as to magnetic metals such as cobalt[40, 41] or nickel.[42] In this case, the absence of surface contamination is deduced from the magnetic properties of the material. The same approach can be used to prepare oxides of nanometric size after oxidation of the metal nanoparticles initially formed.[43] The stabilization of the particles, however, always involves the presence of a stabilizer, whether a polymer or ligands even if some are only loosely coordinated as for example CO and THF in the case of platinum particles.[44, 45] In order to meet the requirements of a microelectronic device, no contaminant should be present in the nanomaterial, since it could potentially alter its electrical properties. We have recently reported the synthesis of unprotected ruthenium particles of various sizes.[46] In this case, the size control is due to the formation of "nanoreactors" in various solvent mixtures. However, the mesoporous nature of these particles make them attractive for catalysis applications but not for microelectronics.

Looking for an alternative approach, we considered a thermolysis reaction leading to the growth of metal particles, but regulated by a competitive sol-gel process leading to the formation of an outer oxide shelter. We describe herein the synthesis and characterization of composite nanoparticles that consist of a core of zero-valent tin surrounded by a thin layer of tin oxides through a mechanism that combines decomposition of an organometallic precursor, controlled surface hydrolysis, and finally oxidation into nanoparticles of $SnO_2$ without coalescence or size change (Scheme 1). We also discuss their use as the sensitive layer in gas sensors. A preliminary account of this work and a patent describing the new materials have been reported.[47, 48]

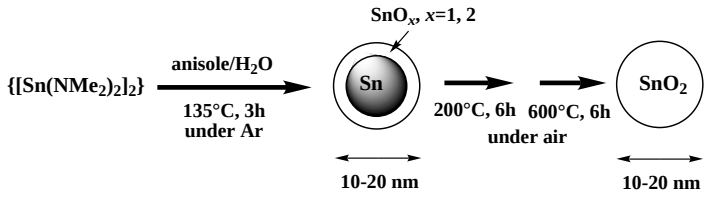


Scheme 1. Schematic representation of the syntheses of tin and tin oxide nanoparticles.

## Results and Discussion

**Synthesis of $Sn/SnO_x$ nanocomposite by thermolysis of $[\{Sn(NMe_2)_2\}_2]$**: The tin precursor chosen for the preparation of the nanoparticles was the bis(dimethylamido)tin(II) dimer $[\{Sn(NMe_2)_2\}_2]$;[49, 50] the choice was made after consideration of thermochemical data which suggested the weakness of the Sn–N bond.[51] $[\{Sn(NMe_2)_2\}_2]$ was prepared according to a published procedure [49, 50] and decomposed in a single step near 190 °C under flowing helium in a thermogravimetric equipment with a weight loss of 55%, consistent with the formation of pure metal residues. Alternative monomeric tin amides ($[Sn(N^iPr_2)_2]$, $[Sn\{N(SiMe_3)_2\}_2]$) were also used as potential precursors in decomposition reactions but did not lead to tractable results.

$[\{Sn(NMe_2)_2\}_2]$ also decomposes slowly in various solvents, either by thermolysis (e.g., at 135 °C) or by reaction with dihydrogen at room temperature. NMR analyses of the reaction products after various reaction times demonstrate that after three hours heating in anisole under argon, all the starting complex has decomposed. When the solvents (THF, toluene, anisole) are rigorously dried, a metallic mirror is produced on the walls of the Fisher–Porter bottle. However, when the thermolysis occurs in anisole in the presence of a small controlled amount of water, the decomposition product consists of a black precipitate.

Transmission electron microscopy (TEM) and high-resolution electron microscopy (HRTEM) studies of samples of nanoparticles prepared from an anisole suspension indicate that the black precipitate consists of agglomerated spherical nanoparticles whose mean size and size distribution depend on the experimental conditions (see below). As a general rule, the 11–20 nm particles are nearly monodisperse in size. High resolution electron microscopy images reveal that these 19 nm nanoparticles have a composite nature of and consist of a well-crystallized zero-valent tin core of $\approx$11 nm diameter covered with a layer $\approx$4 nm thick that is amorphous in appearance (Figure 1).

The outer layer consists of oxidized tin as demonstrated by surface analyses from X-ray photoemission spectroscopy (XPS). The Sn $^3d_{5/2}$ peak (Figure 2) splits into two components with binding energies of 484.7 and 486.4 eV. in a 1:9 ratio. The higher binding energy peak is indicative of $SnO_2$ or SnO, while the lower peak reveals the presence of $Sn^0$.[52] After argon bombardment for five minutes, the same peaks are found in 1:1.5 ratio. This is consistent with the presence of oxidized tin at the surface of the particle and of zero-valent tin in the core of the particle.

Mössbauer spectra of the 19 nm nanoparticles measured at room temperature and at 80 K (Figure 3) clearly indicate the presence of the $\beta$-Sn, together with the $\alpha$-SnO and $SnO_2$ phases. Interestingly, similar phases were previously mentioned in the case of $SnO_x$ thin films obtained by reactive sputtering.[53] The fitted parameters, namely isomer shift,

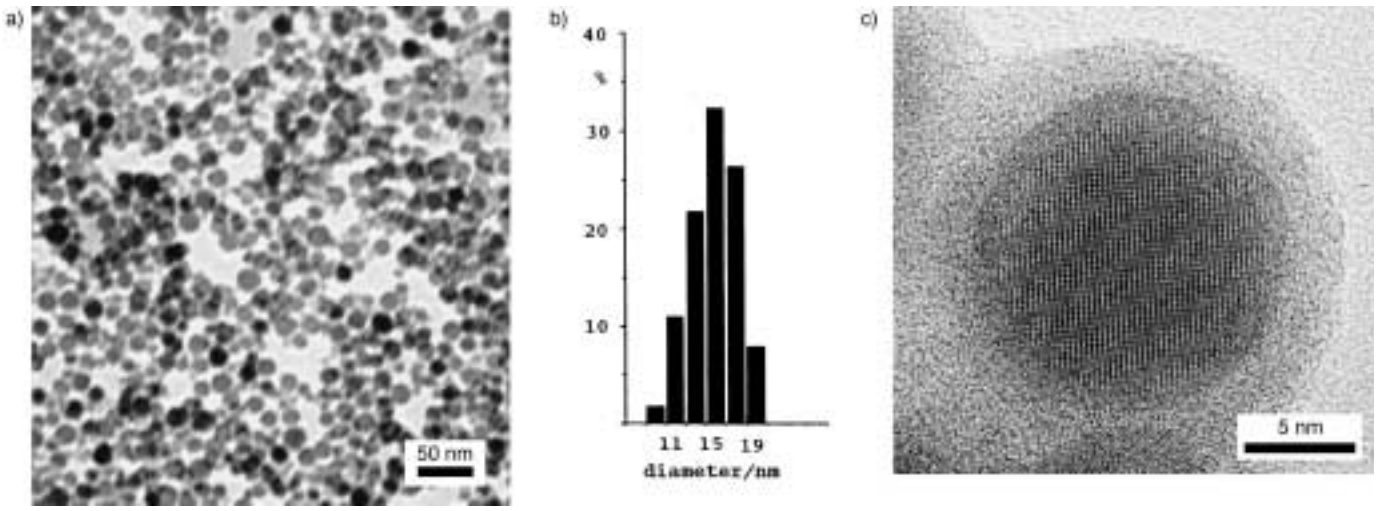


Figure 1. a) TEM image of $Sn/SnO_x$ nanoparticles prepared by thermolysis of $[\{Sn(NMe_2)_2\}_2]$ in wet anisole (28 mmol $L^{-1}$; $[H_2O]/[Sn] = 0.4$; 135 °C; 3 h). b) Histogram of sizes showing the size distribution and detail of one nanoparticle. c) TEM image of the crystallized tin core and the covering layer.

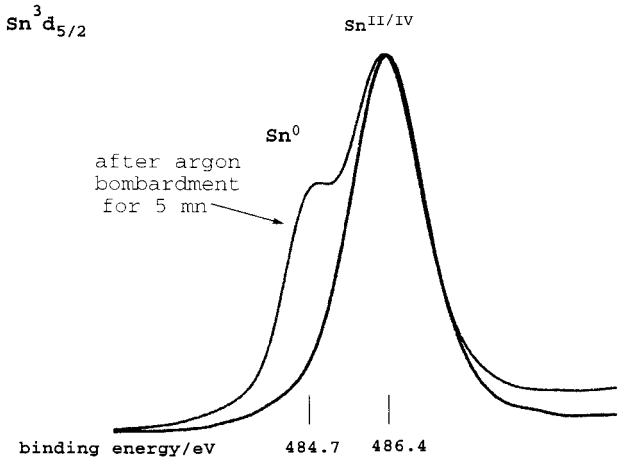


Figure 2. $Sn^3d_{5/2}$ emission peak of the XPS spectrum of $Sn/SnO_x$ nanoparticles.

quadrupole splitting, and linewidth, are listed in Table 1. The $\beta$-Sn component appears as an electric quadrupole singlet with a relative transmission intensity that is strongly temperature dependent. This is consistent with the known important variations with temperature of the recoil-free fraction for $\beta$-Sn. The $\alpha$-SnO component appears as an asymetric quadrupole doublet with a large quadrupole splitting of $\approx 1.4$ $mm^{-1}$. The $SnO_2$ component appears as a quadrupole doublet with isomeric shift around 0 mm $s^{-1}$. This doublet has a quadrupole splitting value of $\approx 0.6$ mm $s^{-1}$, which was previously proposed to arise from the presence of amorphous $SnO_2$.[17] From the Mössbauer spectrum at 80 K and the knowledge of absolute $f$ factor for the oxides ($f_{SnO2}(300\ K) = 0.47 - 0.56$;[54, 55] $f_{SnO}(300\ K) = 0.35$[56]) and Sn metal ($f_{\beta\text{-}Sn}(300\ K) = 0.06$[57]) we could estimate the fraction of oxidized material : $Sn/SnO + SnO_2 = 1/3$. The contributions of the different phases present in the nanoparticles were calculated by comparing Mössbauer peak areas and taking into account the different recoil-free fractions. The tin and oxygen concentrations calculated from the phase distribution measured at 80 K, (88.9 % and 11.1 %, respectively) are in good agreement with those obtained by

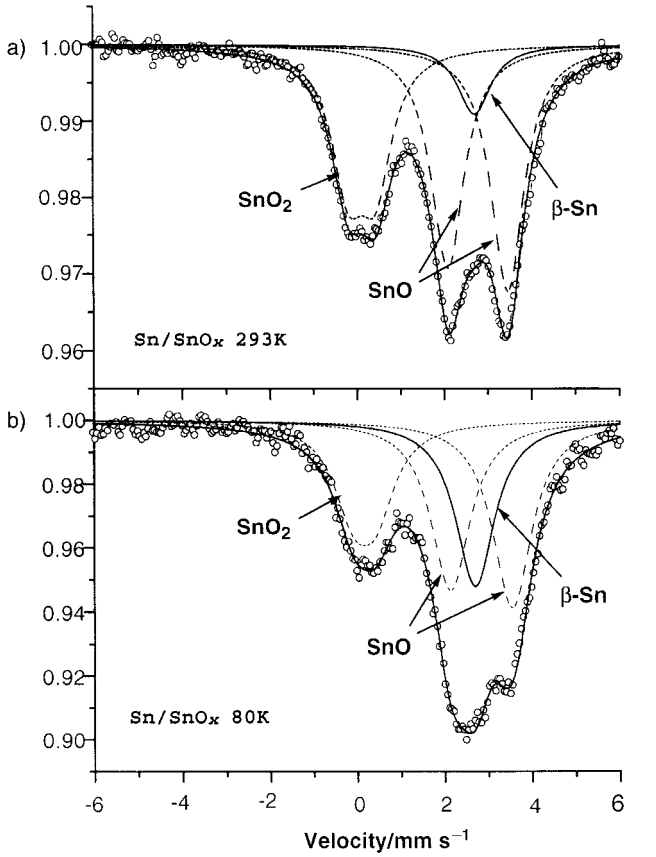


Figure 3. Mössbauer spectra of $Sn/SnO_x$ nanoparticles recorded a) at room temperature and b) at liquid nitrogen temperature.

Table 1. Mössbauer data for tin nanoparticles.

| | $d$ [mm $s^{-1}$] | $\Delta E_Q$ [mm $s^{-1}$] [a] | $\Gamma$[mm $s^{-1}$] | % | species |
|---|---|---|---|---|---|
| 293 K | 0.04(4) | 0.61(5) | 0.94(1) | 33 | $SnO_2$ |
| | 2.59(3) | 0 | 0.95(5) | 9 | $\beta$-Sn |
| | 2.70(3) | 1.38(3) | 0.9(1) | 58 | SnO |
| 80 K | 0.07(2) | 0.52(3) | 1.09(1) | 23 | $SnO_2$ |
| | 2.61(1) | 0 | 1.09(2) | 24 | $\beta$-Sn |
| | 2.74(1) | 1.41(1) | 1.09(5) | 53 | SnO |

[a] Isomer shifts are given with respect to $BaSnO_3$.



0947-6539/00/0622-4084 $ 17.50+.50/0 *Chem. Eur. J.* **2000**, *6*, No. 22

elemental analysis for this sample (90% and 8%, repectively) if we take into account the presence of residual amounts of carbon (1.5%), hydrogen (0.5%) and nitrogen (0.5).

Figure 4 shows the characteristic X-ray diffraction (XRD) pattern of composite $Sn/SnO_x$ nanoparticles. The XRD diagram reveals the $\beta$-Sn phase[58] and the quadratic $\alpha$-SnO phase.[59] This pattern is consistent with particles that have a zero-valent crystalline core and $\alpha$-SnO crystallites in the covering layer. Small unidentified diffraction lines (labeled "x" on Figure 4) were also apparent. Moreover, no line indicating the presence of crystalline $SnO_2$ could be observed; this suggests that tin dioxide is in an amorphous state in these particles.

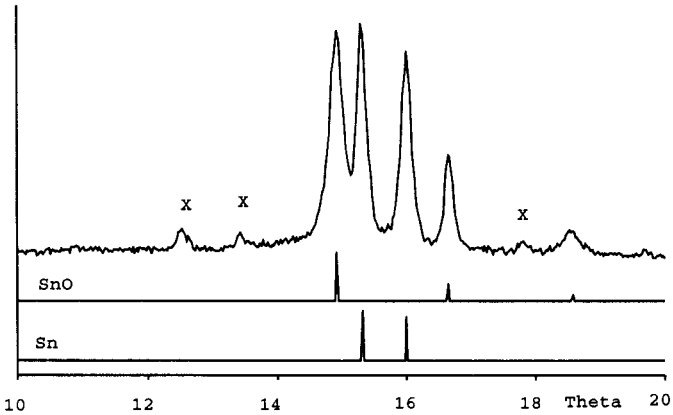


Figure 4. XRD pattern of $Sn/SnO_x$ nanoparticles. x = unidentified diffraction lines.

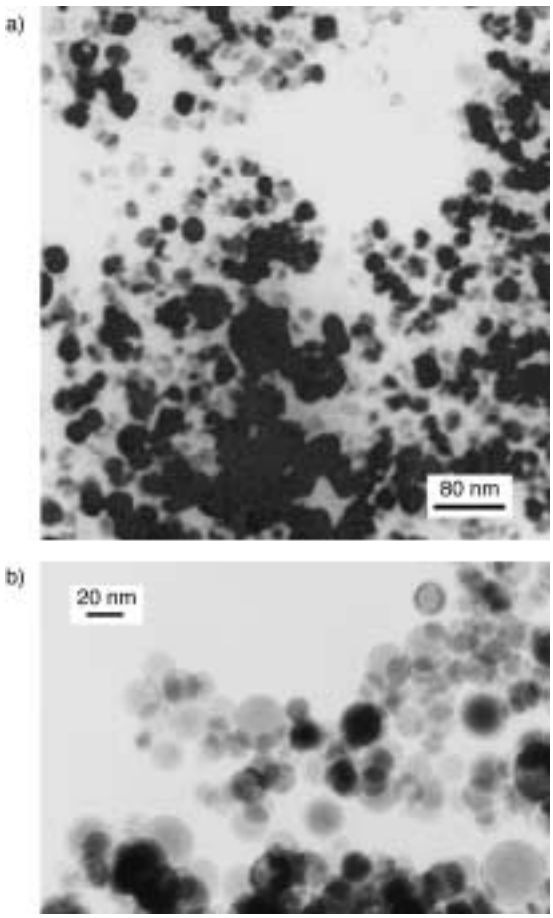


Figure 5. TEM images of nanoparticles prepared by thermolysis of $[\{Sn(NMe_2)_2\}_2]$ in anisole ($28\,mmol\,L^{-1}$; $[H_2O]/[Sn] = 0.06$; 135 °C; 3 h) showing a) bulk tin and b) nanoparticles with broad size distribution.

The dependence of the yield, the composition, the mean size, and the size distribution of the nanoparticles on the initial experimental conditions—temperature, reaction time, and initial content of tin precursor and of water—was investigated both in order to optimize the synthesis and to gain a better understanding of the formation of tin nanoparticles and of their stabilization as a $Sn/SnO_x$ nanocomposite.

First of all, the water content of the solvent was found to be a critical parameter. The yield of nanoparticles, the mean size, and the size distribution are strongly dependent on the initial molar ratio $[H_2O]/[Sn]$. In a rigorously dried solvent, the decomposition product appears as a metallic mirror on the walls of the Fisher–Porter bottle, and no nanoparticles are observed either in the solution or in the solid. We found that the formation of nanoparticles requires the presence of an initial water content in the solvent ranging between the molar ratios $[H_2O]/[Sn]$ 0.06 and 0. 9. For $[H_2O]/[Sn] = 0.06$, the major decomposition product is metallic tin, and the yield of composite nanoparticles is very low. Moreover, the TEM analysis reveals that the nanoparticles obtained display a wide size distribution ranging from 7 to 35 nm (Figure 5). When the water content is increased, the yield in nanoparticles also increases. This is accompanied by a narrowing of the nanoparticles' size distribution and by a slight decrease of their mean diameter (Figure 6). The experimental conditions were optimized for a $[H_2O]/[Sn]$ ratio of 0.4 giving rise to a yield of particles of $\approx 48\%$. Furthermore, the size dispersity is excellent, since 95% of the particles adopt a diameter of between 11 and 19 nm. For higher $[H_2O]/[Sn]$ ratios, the yield of nanoparticles rapidly decreases and a yellowish polymeric tin derivative is formed. This material becomes the sole product of the reaction when the $[H_2O]/[Sn]$ ratio is close to one.

For the optimized water content in the solvent ($[H_2O]/[Sn] = 0.4$), the yield and the mean diameter of the nanoparticles were also found to depend on the initial concentration of the tin precursor, the temperature of decomposition, and the reaction time.

A series of experiments was designed in which these parameters were varied around the values typically used. Combinations of conditions which were varied between the given values for the temperature (110 and 150 °C), time of reaction (1 and 5 h), and the concentration of the tin precursor in anisole (18 and $52\,mmol\,L^{-1}$) were assessed. Thus, the specific effects of each factor have been identified. Temperature appears as a key factor, controlling the formation of protected particles. Indeed, at low temperature, decomposition of the tin precursor occurs but does not lead to the formation of particles. Increase of the time of reaction allows an improvement in the yield of particles and also in the purity of the material, with a decrease in the amount of carbon-containing residues. A slight increase in the particles'

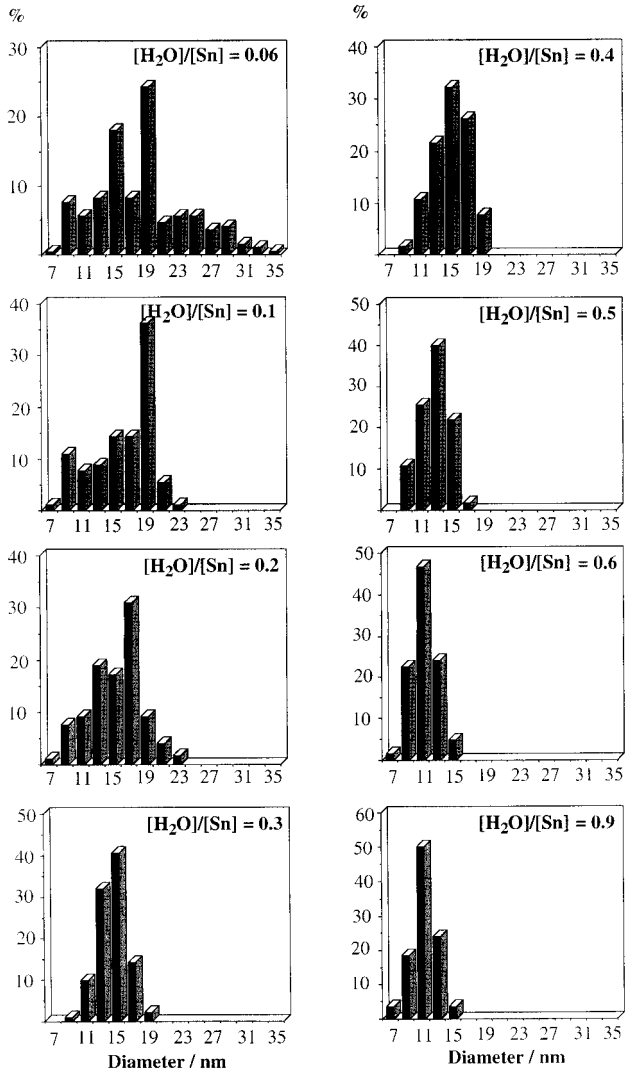


Figure 6. Nanoparticle size distribution as a function of the initial water content of the reaction mixture.

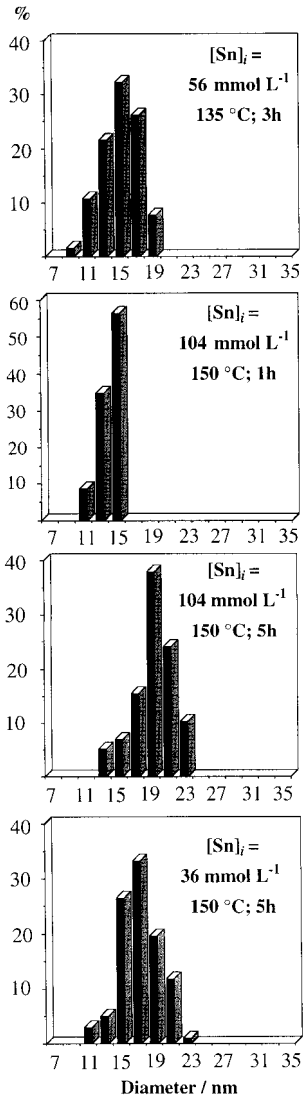


Figure 7. Variations of the nanoparticle size distribution with the initial concentration of tin $[Sn]_i$, temperature of decomposition, and reaction time for the optimal ratio $[H_2O]/[Sn] = 0.04$.

mean diameter was also noted. The main effects of the tin precursor concentration concern i) the yield of particles, which improved with an increase of the concentration, and ii) the mean diameter of the particles, which can be adjusted from 11 nm to 19 nm.

As a general rule, an increase of the values of these parameters is accompanied by an increase of the yield of nanoparticles and of their mean diameter (Figure 7). The optimized conditions were found to be a concentration of $[\{Sn(NMe_2)_2\}_2]$ of 52 mmol $L^{-1}$, a temperature of 150 °C and a reaction time of five hours. Using these optimized conditions, nanoparticles of mean diameter 19 nm were obtained with a yield of 63 %. The size dispersion remains excellent, 93 % of the particles with diameters between 15 and 23 nm, and the degree of purity is high, since less than 1 % of residual carbon is found by microanalysis.

The formation of $Sn/SnO_x$ nanocomposite evidently combines partial hydrolysis and thermolysis of the tin amido precursor. Metal amides are well known to be usually very susceptible to moisture,[51] and we did indeed observe that in presence of water hydrolysis of the amido groups occurs immediately at room temperature to yield dimethylamine[60] and an unidentified tin hydroxide or oxohydroxide. This product may display a crystalline appearance and eventually transforms into tin dioxide after thermal treatment. By analogy with the sol-gel process,[28, 61] we can assume that the replacement of the amido groups by hydroxy groups is followed, upon heating, by condensation reactions that lead to inorganic polymers and eventually oxides. On the other hand, $Sn^0$ particles may be formed upon thermolysis of the Sn–N bonds in dry conditions. This leads, in the rigorous absence of water, to the formation of a metallic mirrored surface and, in the presence of insufficient amounts of water, to large areas that contain zero-valent tin and display a molten appearance (see Figure 5a). The synthesis of these unusual nanoparticles results from two competitive processes that involve the same precursor, namely decomposition and hydrolysis, and, presumably, from the use of the tin hydroxide/oxide formed upon hydrolysis as a ligand to control the growth of the tin particles, in a similar way to what has been observed, for example, for



0947-6539/00/0622-4086 $ 17.50+.50/0 Chem. Eur. J. 2000, 6, No. 22

the growth of platinum metal nanoparticles.[38, 44] This constitutes a new method for the synthesis of composite nanoparticles which may be extended to other semiconducting oxides.

**Synthesis of $SnO_2$ nanoparticles**: The nanocomposite $Sn/SnO_x$ is slowly oxidized in air at room temperature. After a few weeks, the Mössbauer spectrum indicates the presence of predominantly tin dioxide in the material at the expense of tin monoxide and tin $\beta$ phases (Figure 8a and b). In order to reach complete oxidation, the particles were placed either in an oven or in thermogravimetric analysis equipment under flowing dioxygen, heated for six hours at 200 °C, and then heated for a further six hours at 600 °C. The mass increase of the sample is in agreement with the full oxidation of the nanocomposite to $SnO_2$. The Mössbauer spectrum of the oxidized product displayed in Figure 8c corresponds to typical crystalline $SnO_2$ with only one symmetric component that exhibits an electric quadrupole doublet with an isomer shift of 0.0 mm s$^{-1}$ and a quadrupole splitting value of 0.54 mm s$^{-1}$.

The TEM micrograph displayed in Figure 9a shows individual particles that are agglomerated and display the same type of spherical morphology as the non-oxidized particles. Their mean size and the size distribution are unchanged, and in neither case did we observe any sign of coalescence. This is confirmed by atomic force microscope (AFM) and scanning electron microscope (SEM) observations of oxidized particles deposited onto the silicon platform of a chemical sensor microelectronic device (Figure 9b and c); which also provide evidence a porous surface morphology consistent with a large surface area. Interestingly, the AFM data have been obtained on a device that was operated for one month at 500 °C; this demonstrates the stability of the nanomaterial at this temperature.

Figure 10 shows the XRD diagrams of $Sn/SnO_x$ particles (starting material) and of particles deposited on silicon wafers

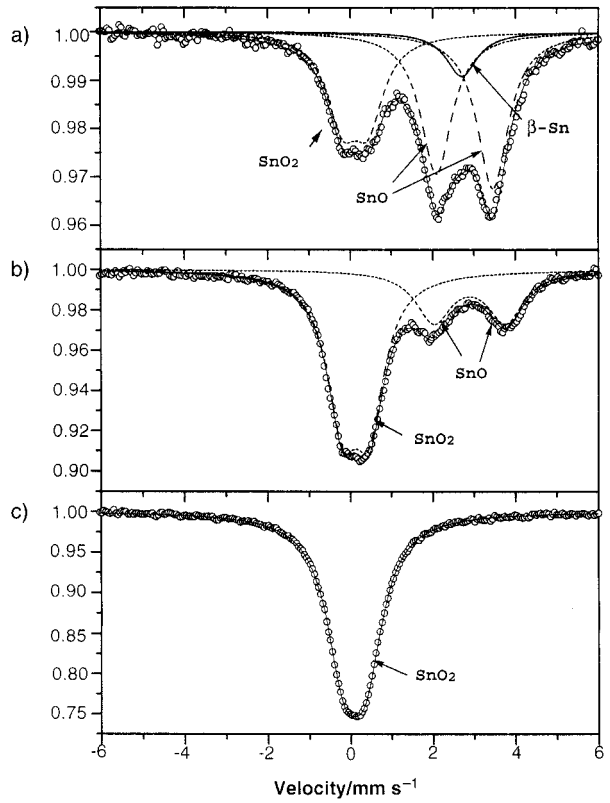


Figure 8. Modification of the Mössbauer spectrum of $Sn/SnO_x$ nanoparticles as a function of oxidation: Mössbauer spectrum of $Sn/SnO_x$ nanoparticles a) after isolation, b) after oxidation for several weeks in air at room temperature, and c) after oxidation in air at 200 °C (6 h) then at 650 °C (6 h).

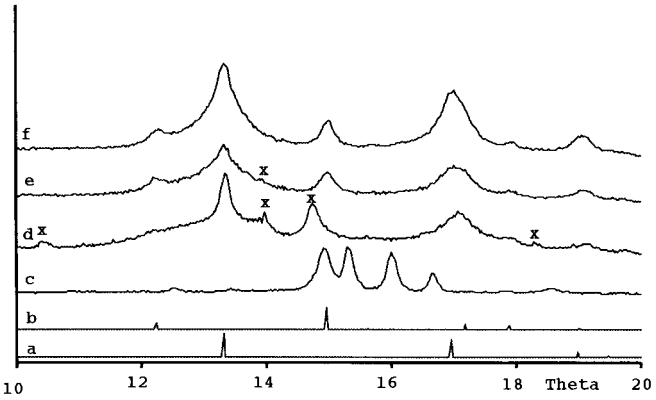


Figure 10. Modification of the XRD pattern of $Sn/SnO_x$ nanoparticles upon aerobic thermal treatments: a) tetragonal $SnO_2$ (cassiterite), b) orthorhombic $SnO_2$, c) initial $Sn/SnO_x$ nanocomposite, d) after oxidation at 450 °C, e) after oxidation at 650 °C, and f) after oxidation at 750 °C. x: unidentified phases.

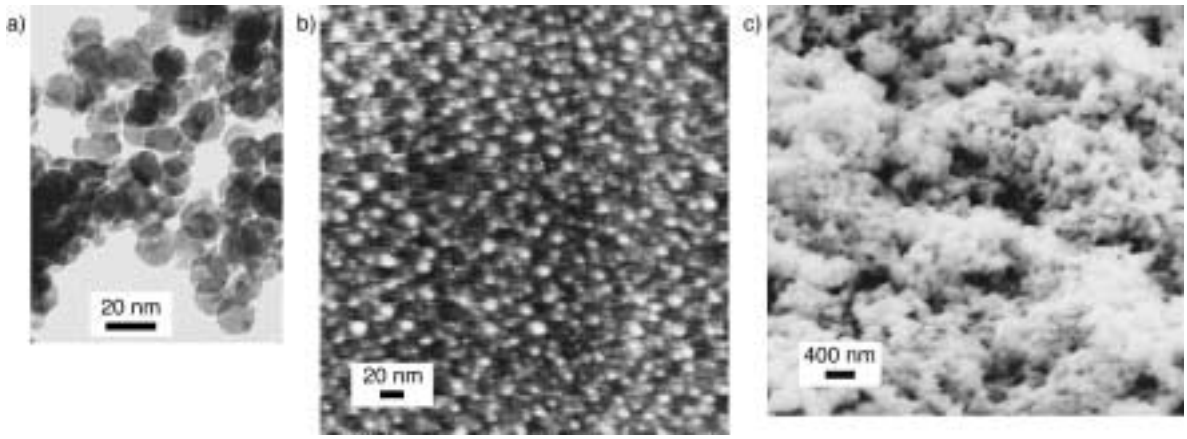


Figure 9. a) TEM, b) AFM, and c) SEM images of nanoparticles of $SnO_2$ prepared by thermal oxidation of the tin nanoparticles $Sn/SnO_x$.

and oxidized at different temperatures. The patterns of the initial $\beta$-Sn and $\alpha$-SnO phases readily disappear at 450 °C to be replaced by the ones of the classical quadratic phase $SnO_2$ (cassiterite)[62] and, to a lesser extent, of the high-pressure orthorhombic phase of $SnO_2$.[63, 64] The latter form has already been observed in the case of $SnO_2$ multilayer thin films grown by the rheotaxial growth and thermal oxidation method (RGTO)[65] or in the case of oxidized tin particles obtained by oxidation of nanophase tin powder.[66, 67] A small amount of unidentified phase (diffraction lines labeled "x" on Figure 10) is detected in the sample oxidized at 450 °C, and disappears at 750 °C.

For confirmation of these results an XPS study of the surface of the oxidized particles was performed. It provides evidence of the presence of oxidized tin (a peak at 486.4 eV for the Sn $^3d_{5/2}$ electrons), and no Sn° was observed, even after argon bombardment. Interestingly, the XPS spectrum for the 1s peak of oxygen (Figure 11) shows two components, one at

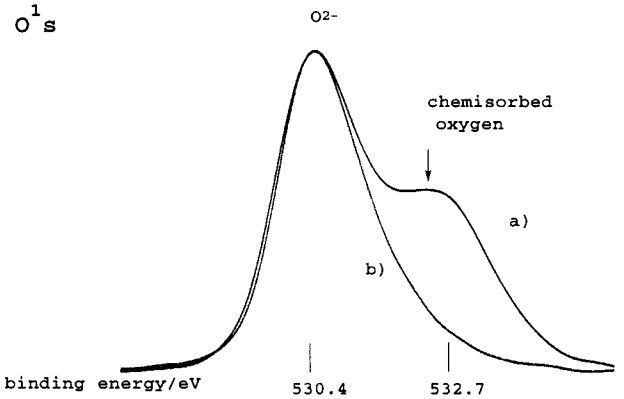


Figure 11. O[1]s emission peaks of the XPS spectrum a) of the tin dioxide nanoparticles and b) of a thin layer of tin dioxide prepared by sputtering.

530.4 eV, which corresponds to oxygen bound to tin, and one at 532.7 eV, which corresponds to adsorbed dioxygen,[68] in a 1.7:1 intensity ratio. This assignment is consistent with argon bombardment experiments which lead to a severe decrease in the peak at 532.7 eV. The relative intensity of the adsorbed dioxygen peak is remarkable when compared with that observed in the case of micronic $SnO_2$ particles synthesized, for example, by sputtering. This result can be directly linked to important differences in surface areas between the two materials. Furthermore, the dioxygen molecules present at the surface of the particles allow the complete oxidation of the surface tin atoms. Upon elimination of the surface dioxygen molecules, in a catalytic oxidation process, for example, or upon substitution of dioxygen by a reducing gas, some electron density is released into the particles that will dramatically modify the conductivity of the material. There is therefore a clear correlation between the amount of surface dioxygen molecules and the gas-sensing sensitivity of $SnO_2$ nanoparticles.[8] This confirms the interest in using nanomaterials for gas detection.

Conductance measurements were performed after deposition of a drop of the composite nanoparticle suspension in anisole between the electrodes of a gas-sensing device integrated onto a silicon platform and in situ oxidation of the nanoparticles. We observed that the resistivity of the $SnO_2$ nanoparticle layer is similar to, or lower than, the resistivity of comparable $SnO_2$-based sensitive layers of gas sensors. Furthermore, the electric properties of this material are strongly sensitive to the presence of a reducing gas, such as carbon monoxide. As shown in Figure 12, the conductance of the sensing layer at 50 °C increases dramatically with the carbon monoxide content of the atmosphere. This behavior is fully reversible. Finally, it is noteworthy that we do not observe a saturation of the particles, which would be detected through a saturation of the conductance, up to 1000 ppm CO.

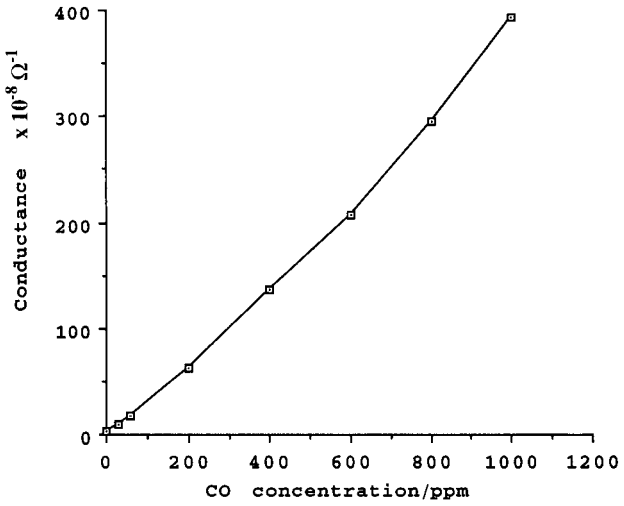


Figure 12. Conductance of a tin dioxide nanoparticle layer as a function of carbon monoxide concentration in air.

## Conclusion

The aim of this study was the synthesis of a new nanomaterial for use as the sensitive layer of gas sensors. For this purpose, we have achieved a high-yield synthesis of monodisperse nanoparticles of Sn/$SnO_x$ through a mechanism involving both the thermal, presumably homolytic, decomposition of the amido precursor and its hydrolysis. The novel aspect of this synthesis is the combination of both types of mechanisms leads to the control of the growth of the particles by the formation of a surface oxide layer in a way similar to the use of coordinating ligands on the surface of metal nanoparticles. This approach has proven not to be limited to tin and is now extended to other metals such as zinc and indium.[71]

The second interesting aspect is that, probably because of the presence of a tin oxide shell, we do not observe any coalescence of the nanoparticles upon heating up to 750 °C. This is in contrast with most observations concerning the preparation of $SnO_2$ thick films, in which coalescence generally occurs. Finally, it is remarkable that this material prepared by using standard solution chemistry procedures is easily integrated onto a microelectronic devices and displays very interesting electronic characteristics when compared with materials obtained by physical techniques, such as sputtering. The mode of integration and the electronic



0947-6539/00/0622-4088 $ 17.50+.50/0 *Chem. Eur. J.* **2000**, *6*, No. 22

characteristics of sensors prepared in this way will be reported in a further, more technical, paper.

In conclusion, this example demonstrates that synthetic procedures typical of organometallic chemistry and leading to high-quality nanomaterials can be used for the preparation of new generations of microelectronic devices. Other applications of similar procedures are presently being studied in our group.

## Experimental Section

**Materials and reagents**: All operations were carried out using standard Schlenk tube or Fischer–Porter bottle techniques under argon. The preparation of the tin precursor $[\{Sn(NMe_2)_2\}_2]$ follows the route described earlier.[49] It was purified by sublimation, and the resulting highly sensitive white crystals were stored under argon at room temperature in a glove-box. Its purity was checked by elemental analysis, mass spectrometry, and $^1H$ NMR spectroscopy. Anhydrous anisole was purchased from Aldrich. THF and toluene were heated under reflux over sodium benzophenone and over sodium, respectively, in nitrogen atmosphere and distilled just before use.

**Synthesis of tin nanoparticles**: In the optimized conditions $[\{Sn(NMe_2)_2\}_2]$ (174 mg, 0.42 mmol) in anisole (8 mL) containing traces of water (0.4 mg mL$^{-1}$ of anisole; 0.17 mmol) were heated at 150 °C under magnetic stirring in a Fischer–Porter bottle. The initial light yellow solution darkened within 15 min and a black solid progressively precipitated. After 5 hours, the solution was removed by filtration, and the black precipitate was washed with anisole ($3 \times 10$ mL) and dried under vacuum (86.3 mg). Elemental analysis (%): Sn 73.06, O 13.45, C 1.8, H 0, N 0.25; TEM analysis: nanoparticles, size: 14–23 nm, mean size: 19 nm; yield: 63 %.

**Influence of the water content**: In a series of eight experiments, the decomposition of $[\{Sn(NMe_2)_2\}_2]$ (174 mg; 0.42 mmol) was achieved at 135 °C in dry anisole (16 mL) to which was added known amounts of water so that the initial ratio $[H_2O]/[Sn]$ was0.06, 0.1, 0.2, 0.3, 0.4, 0.5, 0.6, and 0.9, respectively. The water content of the solvent was checked by Karl–Fisher volumetric titration by using Mettler equipment prior to dissolution of the tin precursor. After 3 hours, the resulting heterogeneous reaction mixtures were cooled to room temperature. With the exception of the water-rich solutions, a dark brown–black precipitate was formed and separated from a cloudy light yellow supernating solution by filtration. Moreover, a metallic mirror was observed on the wall of the Fischer–Porter bottle for the solutions containing less water (i.e., those for which $[H_2O]/[Sn] = 0.06$, 0.1, and 0. 2). The precipitates were washed with dry anisole ($3 \times 10$ mL) and sampled for TEM analysis. For $[H_2O]/[Sn] = 0.6$ and 0.9, an orange–brown polymer formed and was separated by decantation and filtration. It was washed with anisole and sampled for SEM and TEM analyses. Elemental analyses of dry samples indicated tin contents of 81.3 and 83.3 %, respectively.

**Influence of concentration, temperature and reaction time**: In a series of eight experiments, the thermolysis of the tin precursor (174 mg; 0.42 mmol) was performed in wet anisole ($[H_2O]/[Sn] = 0.4$) and employing all the different possible combinations between the given values for the temperature (110 and 150 °C), reaction time (1 and 5 hours), and initial concentration of the precursor (18 and 52 mmol L$^{-1}$). The products of the reaction were fully characterized by SEM and TEM analyses. The resulting black precipitate was isolated and its composition was determined by microanalysis.

**Thermogravimetric analyses and microanalyses**: Thermogravimetric analyses (TGA) were obtained on a SETARAM TG-DTA 92 instrument. Microanalyses were performed by the "service de Microanalyses du Laboratoire de Chimie de Coordination" (C, H, N) or by the "Service central de Microanalyses du CNRS" (Sn, O).

**Electron microscopy experiments**: Samples for TEM and HREM studies were prepared in a glove-box by slow evaporation of a drop of suitably diluted colloidal suspensions deposited on holey carbon-covered copper grids. The TEM experiments were performed at the "Service Commun de Microscopies de l'Université Paul Sabatier" on a JEOL JEM 200CX-T electron microscope working at 200 kV and a Philips CM 12 electron microscope working at 120 kV with respective point resolutions of 4.5 and 5 Å. High-resolution images were observed with a JEOL JEM 2010 electron microscope working at 200 kV with a point resolution of 2.5 Å. The size distribution of the particles was determined from enlarged photographs by measuring about 200 particles for each sample. The SEM and AFM direct observations of the tin dioxide layer deposited on the silicon platform of the device were performed on a PHILIPS XL40 FEG and a NANOSCOPE II instrument, respectively.

**X-ray photoelectron spectroscopy experiments**: Samples for XPS studies were prepared in a glove-box by slow evaporation of a nanoparticle suspension deposited on a 1 cm$^2$ silicon support. The spectra were recorded on a VG ESCALAB MKII spectrometer with $Mg_{K\alpha}$ radiation.

**X-ray powder diffraction**: XRD profiles of the particles were measured with a SEIFERT XRD 3000 TT X-ray diffractometer with $Cu_{K\alpha}$ radiation. The data were collected in the $\Theta/\Theta$ configuration in the case of the $Sn/SnO_x$ powder, and the grazing incidence configuration in the case of $SnO_2$ deposited on silicon wafers.

**Mössbauer experiments**: Measurements were performed at room temperature and at 80 K against a $Ba^{119}Sn^mO_3$ source with a conventional constant acceleration spectrometer. The velocity scale was calibrated with a magnetic sextet of a high purity iron-foil absorber with $^{57}Co(Rh)$ as source. Recorded spectra were then fitted to lorentzian line shape by usual least-square methods.[69] Isomer shifts are quoted with respect to the center of the $BaSnO_3$ spectrum obtained with the same source.

**Thermal oxidation of tin nanoparticles and conductivity measurements**: Anisole suspensions of the $Sn/SnO_x$ nanocomposite were dropped onto a silicon platform of a chemical sensor device integrating all structures that are needed to receive and make operational a sensing layer (heater, metal interconnects, membrane, insulating layer, etc.).[70] After drying, the resulting thick film (thickness: 2 μm) was heat-treated in air for a 135 min period at temperatures ranging from 50 to 525 °C prior to testing. The sensor heating was controlled by a constant-voltage power supply. The surface morphology of the films was characterized by means of SEM and AFM experiments. The conductivity measurements were carried out under controlled gaseous atmosphere and temperature on a home-made test bench by using interfacing hardware. The data acquisition was controlled through Labview software (National Instruments).

## Acknowledgements

The authors are grateful to V. Colliere for assistance with the electronic microscopy (Service Commun de Microscopie Électronique de l'Université Paul Sabatier), to G. Chatainier for XPS spectra (ENSCT-INP), and to Dr. R. Corratger for AFM (CEMES-CNRS). This work is supported by funds from MOTOROLA SA, MicroChemical Systems SA, CNRS, and Région Midi-Pyrénées.

[1] S. Fujitsu, H. Toyoda, H. Yanagida, *J. Am. Ceram. Soc.* **1987**, *70*, C71.
[2] S. Fujitsu, K. Koumoto, H. Yanagida, *Solid State Ionics* **1989**, *32/33*, 482.
[3] N. Raghu, T. R. N. Kutty, *Appl. Phys. Lett.* **1992**, *60*, 100.
[4] "Characterization and Reactivity of Molecular Oxygen Species on Oxide Surfaces", M. Che, A. J. Tench, *Advances in Catalysis* (Eds: D. D. Eley, H. Pines, P. B. Weisz) Academic Press, New York, **1983**.
[5] A. Bielanski, J. Haber, *Oxygen in Catalysis*, Marcel Dekker, New York, **1991**.
[6] "Chemical and Biochemical Sensors", *Sensors: A Comprehensive Survey*, *Vol. 3* (Eds: W. Göpel, J. Hesse, J. N. Zemel, T. A. Jones, M. Kleitz, I. Lundström, T. Seiyama), VCH, Weinheim, **1992**.
[7] G. Sberveglieri, *Gas Sensors: Principles*, *Operation and Developments*, Kluwer Academic, Dordrecht, Boston, London, **1992**.
[8] K. Ihokura, J. Watson, *The Stannic Oxide Gas Sensor: Principles and Applications*, CRC, Boca Raton, **1994**.
[9] N. Yamazoe, *Sens. Actuators B* **1991**, *5*, 7.
[10] C. Xu, J. Tamaki, N. Miura, N. Yamazoe, *Sens. Actuators B* **1991**, *3*, 147.
[11] X. Wang, S. S. Yee, W. P. Carey, *Sens. Actuators B* **1995**, *24/25*, 454.

  0947-6539/00/0622-4089 $ 17.50+.50/0 

[12] Y. Shimizu, M. Egashira, *MRS Bull.* **1999**, *24*, 18.
[13] S. Sakohara, L. D. Tickanen, M. A. Anderson, *J. Phys. Chem.* **1992**, *96*, 11086.
[14] T. W. Capehart, S. C. Chang, *J. Vacuum Sci. Technol. B* **1981**, *18*, 393.
[15] G. Micocci, A. Serra, P. Siciliano, A. Tepore, Z. Ali-Adib, *Vacuum* **1996** ,*47*, 1175.
[16] D. G. Rickerby, M. C. Horillo, J. P. Santos, P. Serrini, *Nanostruct. Mater.* **1997**, *9*, 43.
[17] F. C. Stedile, B. A. S. de Barros, C. V. Barros Leite, F. L. Freire, Jr., I. J. R. Baumvol, W. H. Schreiner, *Thin Solid Films* **1989**, *170*, 285.
[18] V. Demarne, A. Grisel, *Sens. Actuators B* **1993** ,*15 – 16*, 63.
[19] G. Gaggiotti, A. Galdikas, S. Kaciulis, G. Mattogno, A. Setkus, *J. Appl. Phys.* **1994**, *76*, 4467.
[20] G. Sberveglieri, *Sens. Actuators B* **1992**, *6*, 239.
[21] H. Ogawa, A. Abe, M. Nishikawa, S. Hayakawa, *J. Electrochem. Soc.* **1981**, *128*, 685.
[22] H. Ogawa, A. Abe, M. Nishikawa, S. Hayakawa, *J. Electrochem. Soc.* **1981**, *128*, 2020.
[23] G. Williams, G. S. V. Coles, *J. Mater. Chem.* **1998**, *8*, 1657.
[24] G. Williams, G. S. V. Coles, *MRS Bull.* **1999**, *24*, 25.
[25] L. Bruno, C. Pijolat, R. Lalauze, *Sens. Actuators B* **1994** ,*18 – 19*, 195.
[26] Y. Liu, W. Zhu, O. K. Tan, X. Yao, Y. Shen, *J. Mater. Sci.* **1996** *7*, 279.
[27] M. Ocana, E. Matijevic, *J. Mater. Res.* **1990**, *5*, 1083.
[28] M. J. Hampden-Smith, T. A. Wark, C. J. Brinker, *Coord. Chem. Rev.* **1992**, *112*, 81.
[29] M. Ocana, C. J. Serna, E. Matijevic, *Colloid Polym. Sci.* **1995**, *273*, 681.
[30] A. Dieguez, A. Romano-Rodriguez, J. R. Morante, U. Weimar, M. Schweizer-Berberich, W. Goepel, *Solid State Phenom.* **1996**, *51 – 52*, 441.
[31] S.-S. Park, J. D. Mackenzie, *Thin Solid Films* **1996**, *274*, 154.
[32] M. I. Ivanovskaya, P. A. Bogdanov, D. R. Orlik, A. C. Gurlo, V. V. Romanovskaya, *Thin Solid Films* **1997**, *296*, 41.
[33] S. G. Ansari, P. Boroojerdian, S. R. Sainkar, R. N. Karekar, R. C. Aiyer, S. K. Kulkarni, *Thin Solid Films* **1997**, *295*, 271.
[34] A. Dieguez, A. Romano-Rodriguez, J. R. Morante, U. Weimar, M. Schweizer-Berberich, W. Goepel, *Sens. Actuators B* **1996** ,*B31*, 1.
[35] S. R. Davis, A. V. Chadwick, J. D. Wright, *J. Mater. Chem.* **1998**, *8*, 2065.
[36] G. Beensh-Marchwicka, L. Krol-Stepniewska, A. Misiuk, *Thin Solid Films* **1984**, *113*, 215.
[37] J. S. Bradley, J. M. Millar, E. W. Hill, C. Klein, B. Chaudret, A. Duteil, *Faraday Discuss. Chem. Soc.* **1991**, *92*, 255.
[38] A. Duteil, R. Quéau, B. Chaudret, R. Mazel, C. Roucau, J. S. Bradley, *Chem. Mater.* **1993**, *5*, 341.
[39] C. Amiens, D. de Caro, B. Chaudret, J. Bradley, R. Mazel, C. Roucau, *J. Am. Chem. Soc.* **1993**, *115*, 11638.
[40] J. Osuna, D. de Caro, C. Amiens, B. Chaudret, E. Snoeck, M. Respaud, J. M. Broto, A. R. Fert, *J. Phys. Chem.* **1996**, *100*, 14571.
[41] M. Respaud, J. M. Broto, H. Rakoto, A. R. Fert, L. Thomas, B. Barbara, M. Verelst, E. Snoeck, P. Lecante, A. Mosset, J. Osuna, T. Ould-Ely, C. Amiens, B. Chaudret, *Phys. Rev. B* **1998**, *57*, 2925.
[42] T. Ould-Ely, C. Amiens, B. Chaudret, E. Snoeck, M. Verelst, M. Respaud, J.-M. Broto, *Chem. Mater.* **1999**, *11*, 526.
[43] M. Verelst, T. Ould-Ely, C. Amiens, E. Snoeck, P. Lecante, A. Mosset, M. Respaud, J.-M. Broto, B. Chaudret, *Chem. Mater.* **1999**, *11*, 2702.
[44] A. Rodriguez, C. Amiens, B. Chaudret, M. J. Casanove, P. Lecante, J. S. Bradley, *Chem. Mater.* **1996**, *8*, 1978.
[45] F. Dassenoy, K. Philippot, T. Ould-Ely, C. Amiens, P. Lecante, E. Snoeck, A. Mosset, M.-J. Casanove, B. Chaudret, *New J. Chem.* **1998**, *22*, 703.
[46] O. Vidoni, K. Philippot, C. Amiens, B. Chaudret, O. Balmes, J.-O. Malm, J.-O. Bovin, F. Senocq, J. Casanove, *Angew. Chem.* **1999**, *111*, 3950; *Angew. Chem. Int. Ed.* **1999**, *38*, 3736.
[47] P. Fau, C. Nayral, B. Chaudret, A. Maisonnat (Motorola Semiconductors SA), European patent No. 98400246.9 – 2104, filing date 05/02/1998; [*Chem. Abs.* **1999**, *131*, 237320].
[48] C. Nayral, T. Ould-Ely, A. Maisonnat, B. Chaudret, P. Fau, L. Lescouzeres, A. Peyre-Lavigne, *Adv. Mater.* **1999**, *11*, 61.
[49] P. Foley, M. Zeldin, *Inorg. Chem.* **1975**, *14*, 2264.
[50] M. M. Olmstead, P. P. Power, *Inorg. Chem.* **1984**, *23*, 413.
[51] M. F. Lappert, P. P. Power, A. R. Sanger, R. C. Srivastava, *Metal and Metalloid Amides*, Ellis Horwood, Chichester, **1980**.
[52] *Handbook of X-Ray Photoelectron Spectroscopy*, (Eds.: C. D. Wagner, W. M. Riggs, L. E. Davis, J. F. Moulder, G. E. Muilenberg), Perkin Elmer, Eden Prairie, MN, **1979**.
[53] E. Leja, J. Korecki, K. Krop, K. Toll, *Thin Solid Films* **1979**, *59*, 147.
[54] J. L. Solis, J. Frantti, V. Lantto, L. Häggström, M. Wikner, *Phys. Rev. B* **1998**, *57*, 13941.
[55] M. S. Moreno, R. C. Mercader, *Phys. Rev. B* **1994**, *50*, 9875.
[56] C. Hohenemser, *Phys. Rev.* **1965**, *139*, A185.
[57] R. H. Herber, *Phys. Rev. B* **1983**, *27*, 4013.
[58] *Joint Committee on Powder Diffraction Standards (JCPDS)*, *International Center of Diffraction Data*, Swarthmore, PA, USA, **1992**, file 4 – 673.
[59] *Joint Committee on Powder Diffraction Standards (JCPDS)*, *International Center of Diffraction Data* , Swarthmore, PA, USA **1992**, file 6 – 395.
[60] This was clearly demonstrated by proton NMR spectrum of a $C_6D_6$ solution of $[\{Sn(NMe_2)_2\}_2]$ which exhibits a sharp singlet at $\delta = 2.20$ for the methyl proton of $HNMe_2$ when small amount of water was added.
[61] J. Livage, M. Henry, C. Sanchez, *Prog. Solid State Chem.* **1988**, *18*, 259.
[62] *Joint Committee on Powder Diffraction Standards (JCPDS)*, *International Center of Diffraction Data*, Swarthmore, PA, USA **1992**, file 41 – 1445.
[63] K. Suito, N. Kawai, Y. Masuda, *Mater. Res. Bull.* **1975**, *10*, 677.
[64] *Joint Committee on Powder Diffraction Standards (JCPDS)*, *International Center of Diffraction Data*, Swarthmore, PA, USA **1992**, file 29 – 1484.
[65] L. E. Depero, C. Perego, L. Sangaletti, G. Sberverglieri, *X-ray Diffraction and Modelling Studies of Multilayer $SnO_2$ Thin Film Gas Sensors* (Eds.: H. J. Frost, C. A. Ross, M. A. Parker, E. A. Holm), MRS, Boston, **1996**.
[66] M.-Y. Huh, S.-H. Kim, J.-P. Ahn, J.-K. Park, B.-K. Kim, *Nanostruct. Mater.* **1999**, *11*, 211.
[67] C. H. Shek, J. K. L. Lai, G. M. Lin, Y. F. Zheng, W. H. Liu, *J. Phys. Chem. Solids* **1996**, *58*, 13.
[68] K. S. Yoo, N. W. Cho, H. S. Song, H. J. Jung, *Sens. Actuators B* **1995**, *24 – 25*, 474.
[69] W. Künding, *Nucl. Instrum. Methods* **1969**, *75*, 336.
[70] C. Nayral, B. Chaudret, A. Maisonnat, P. Fau, L. Lescouzeres (MicroChemical Systems SA), French patent No 99 – 088749, filing date 02/07/1999.
[71] F. Rataboul, K. Soulantika, A. Maisonnat, B. Chaudret, unpublished results.

Received: February 21, 2000 [F2313]

  0947-6539/00/0622-4090 $ 17.50+.50/0 